Seismic vulnerability assessment of precast post-tensioned segmental bridge piers subject to far-fault ground motions

Ehsan Ahmadi[1] **, *Mohammad M. Kashani*[2]
1. School of Engineering and the Built Environment, Birmingham City University, UK
2. Faculty of Engineering and Physical Sciences, University of Southampton, UK
** Corresponding Author, email: ehsan.ahmadi@bcu.ac.uk*

Abstract

Precast post-tensioned segmental (PPS) bridge piers mitigate global and local damages of bridge structures through natural hinges (joints between their segments) and rocking motion of their segments. The application of the PPS piers is currently growing in Accelerated Bridge Construction (ABC) where the segments are manufactured offsite with higher quality, and are assembled onsite in a short time. Structural vulnerability analysis of the PPS piers is very essential in extending their engineering implementation under seismic loading. Thus, this work particularly focuses on seismic vulnerability assessment of the PPS piers. To achieve this goal, a previously developed and experimentally validated robust Finite Element model of the PPS piers in OpenSees programme is used to analyse PPS piers of various aspect ratios. An equivalent reinforced concrete (RC) pier to one of the PPS piers is also analysed. Incremental Dynamic Analysis (IDA) is performed and fragility curves are generated to evaluate seismic performance of the PPS piers and an equivalent RC pier using a suite of 44 far-fault ground motions. The IDA results show that slenderising the PPS pier tends to change the failure criterion from the yielding of the post-tensioning tendon to the strength loss of the pier. For squat and slender piers, the yielding of the tendon governs the failure of the pier while the strength of very slender PPS piers drops due to second-order effects at small drift values prior to the yielding of the post-tensioning tendon. It is also found from fragility curves that squat piers are more prone to seismic collapse compared to slender piers. The equivalent RC pier reaches slight and medium damage states in lower intensity measures compared to the PPS pier.

Keywords: Precast post-tensioned segmental columns; accelerated bridge construction; incremental dynamic analysis; far-fault ground motions; seismic performance assessment

1. Introduction

1.1 Background

Conventional cast-in-place (CIP) reinforced concrete (RC) piers are monolithically constructed and attached to their foundation. The concrete cracks, and reinforcing bars yield and buckle under lateral extreme loadings. This is mostly occurring at the base piers where the largest shear force and bending moment coexist. At low-amplitude lateral loading, the concrete cracking results in exposing reinforcing bars to harsh chloride environments leading to highly likely unserviceability or collapse of the whole bridge structure ([1], [2], [3]). To reach a more resilient bridge structure (i.e. low damage probability and longer service life), the precast post-tensioned segmental (PPS) piers have received much attention as an excellent alternative to the CIP piers in recent years. Offsite manufacturing of the segments of the PPS piers results in a higher concrete quality, shorter construction time, and ease of construction. Additionally, the rocking mechanism of the segments avoids large concrete cracks, and post-tensioned stainless steel tendon provides self-centring ability of the pier under lateral seismic loading. The pier's resistance in exposure to aggressive environment is also improved due to the high corrosion resistance of stainless steel. It should be noted that the self-centring and rocking mechanisms have also been used in steel frames ([4], [5]).

1.2 Previous Studies

Far before emergence of the idea of the PPS pier, the rocking motion of rigid blocks has been investigated. Many researchers studied rocking motion of a rigid block subject to harmonic base excitation ([6],[7],[8],[9],[10],[11]). Nonlinear mechanics of these single blocks were also examined under seismic ground motions ([12],[13],[14],[15]). Some other studies investigated single and multiple rigid blocks to simulate rocking motion and stability of art objects subject to impulse excitations ([16],[17],[18],[19]).

A large number of laboratory researches have investigated structural behaviour of the PPS piers mainly under quasistatic cyclic loading and infrequently dynamic excitations ([20],[21],[22],[23]). Hewes [24] examined structural performance of the PPS piers with various aspect ratios through a number of cyclic tests. It was found that the PPS piers have pronounced resistance against seismic loading while having low energy-dissipating capacity. To improve energy-dissipating capacity of the PPS piers, many methods were suggested throughout quasistatic and cyclic testing protocols ([25],[26],[27],[28],[29]). In some cases, shake table testings including actual ground motions as base excitations were conducted to investigate seismic performance of the PPS piers equipped with external attachments for energy dissipation ([30],[31],[32]). Recently, shake table tests using sweep sine base excitations were carried out on small-scale segmental columns with layers of high-damping materials placed between their segments ([33],[34],[35],[36]).

In addition to the laboratory researches, many numerical simulations have been performed on the PPS piers. 3D continuum finite element (FE) models ([25],[29],[37],[38],[39],[40]) and fibre-based FE models ([41],[42]]) were developed to determine dynamic demands of the PPS piers. The continuum FE models are able to reliably simulate local damages at the compression zones of the contact surfaces between the segments. However, these models lack calculation efficiency particularly in case of nonlinear time history analysis where a large number of ground motions are intended to be used. The fibre-based FE models have been widely employed in seismic response simulation of the RC piers ([43],[44],[45]). The fibre-based FE models are computationally more efficient compared to the continuum FE models. Nevertheless, the fibre-based FE models are unable to realistically simulate the contact surface and compression zones between segments of the PPS piers, i.e. rocking joints and compression zones, as accurate as the continuum FE models. Simplified analytical models ([26],[25]) were also developed to predict cyclic behaviour of the PPS piers. Cai et al. [46] studied the effects of crucial parameters on residual drifts of the PPS piers equipped with ED bars. Most of these numerical models were used to validate experimental results focusing only on quasi-static and cyclic behaviour of the PPS piers. In a new study, Ahmadi and Kashani [47] developed a computationally efficient FE model for the PPS piers in OpenSees programme [48] where the segments were modelled as elastic blocks and the contact surfaces were simulated using a number of zero-tension elastic springs. The model was experimentally validated throughout a number of quasi-static and shake table tests. To sum up, while the seismic behaviour of the PPS piers have been investigated both experimentally and numerically for a single or a few ground motions, more robust and reliable nonlinear dynamic analyses for a large number of ground motion records are required to probabilistically describe seismic performance of the PPS piers. This needs a high-fidelity and computationally-efficient structural model of the pier and an extensive suit of ground motion records where each record is scaled to various levels of intensity to monitor linear to nonlinear behaviour of the piers.

1.3 Contribution

As the above literature survey demonstrated, even though quasistatic and cyclic behaviour of the PPS piers have received much attention, their seismic performance subject to an ensemble of actual ground motion records yet to be quantified using advanced nonlinear dynamic analyses. Therefore, this study focuses on seismic performance assessment of the PPS piers using Incremental Dynamic Analysis (IDA) tool for the first time [49]. To reach this goal, an experimentally-validated and highly efficient numerical model in OpenSees programme [48] is used to analyse three PPS piers with different aspect ratios. An equivalent RC pier to one of the PPS piers is also modelled to be compared with the PPS pier. Using pushover analysis results of the piers, potential failure mechanisms of the PPS piers and the equivalent RC pier are investigated and identified. Using the analyses results a set of new seismic damage limit states are defined for PPS piers, which are key factors in their seismic design and fragility analysis. Then, IDA curves and fragility curves of the PPS piers as well as the equivalent RC pier are generated subject to 44 far-fault ground motion records.

2. The Numerical Modelling of Piers

2.1 The PPS piers

Three PPS piers of different aspect ratio are used in this work. As shown in Figure 1, the PPS piers constitute n precast concrete segments of width B and total height of H, and support a bridge deck on top of the segments. The axial load from the top deck is defined as a ratio of the axial load to axial capacity of the concrete section, $N/(f_cA_g)$, where N is the axial load, f_c and A_g are the concrete compressive strength and the total cross section area of each pier, respectively. The segments are tightened together by a post-tensioning stainless steel tendon, fixed at the base and at the top of the pier. The unbonded tendon provides a self-centring mechanism in the pier under lateral loading scenarios.

Table 1 summarises the properties of the piers used in this study. The piers consist of 2, 4, and 8 square segments with heights of 1, 2, and 3 m, which represent squat, slender, and very slender PPS piers. The post-tensioning tendon ratios, $\rho = A_t/A_g$ (tendon-to-segment area ratio), of 0.005, 0.01, and 0.02 are considered respectively for the 2, 4, and 8-segment piers such that all piers have the same stiffness for the tendon, E_tA_t/H. E_t and A_t are the elastic modulus and area of the tendon respectively. Constant axial load ratio, $N/(f_cA_g) = 0.2$, and initial post-tensioning-to-yield stress ratio, $\sigma_0^t/\sigma_y = 0.4$, are selected for the tendon of the piers.

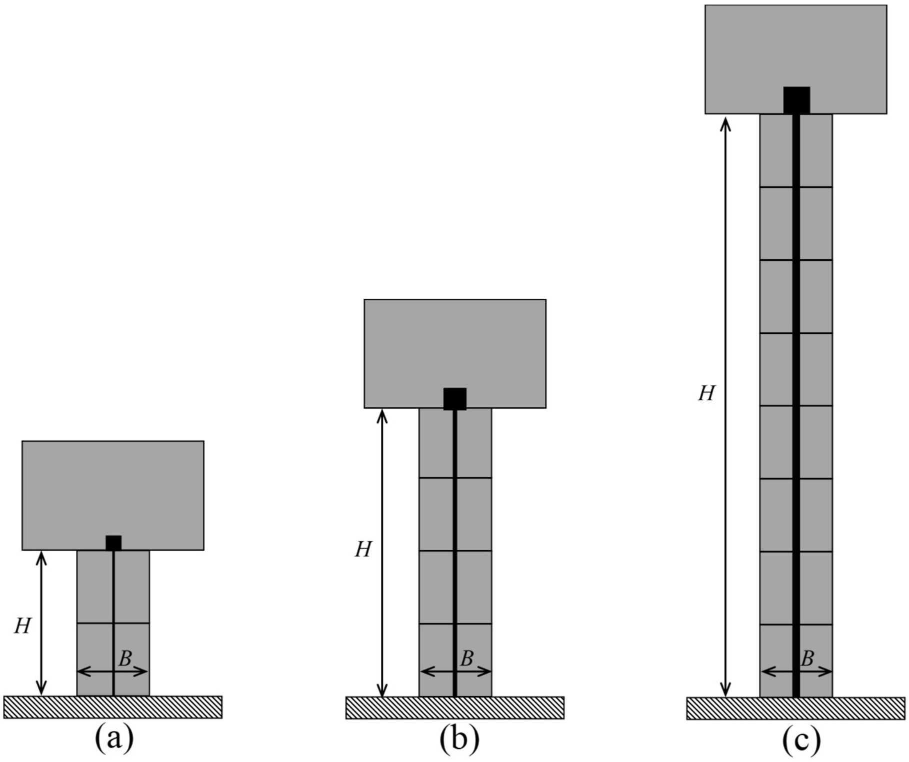

Figure 1. Schematic view of the PPS piers used in this study: (a) 2 segments, C2 (b) 4 segments, C4, and (c) 8 segments, C8.

Table 1. Details of the PPS piers used in this study.

Column Label.	n (number of segments)	H (m)	B (m)	ρ	$N/(f_c A_g)$	σ_0^t/σ_y
C2	2	1	0.5	0.005	0.2	0.4
C4	4	2	0.5	0.01	0.2	0.4
C8	8	4	0.5	0.02	0.2	0.4

To simulate nonlinear seismic behaviour of the PPS piers under different ground motions, a 2D Finite Element model made in OpenSees programme is used (see Figure 2). As shown in Figure 2b, the segments were modelled using Elastic Beam-Column elements with no sliding behaviour, and the post-tensioning stainless steel tendon was modelled with a Truss Element. An Elastic Perfectly Plastic material was used to model the tendon, and an initial tensile strain was included in the Elastic Perfectly Plastic material model to consider the post-tensioning effect of the tendon.

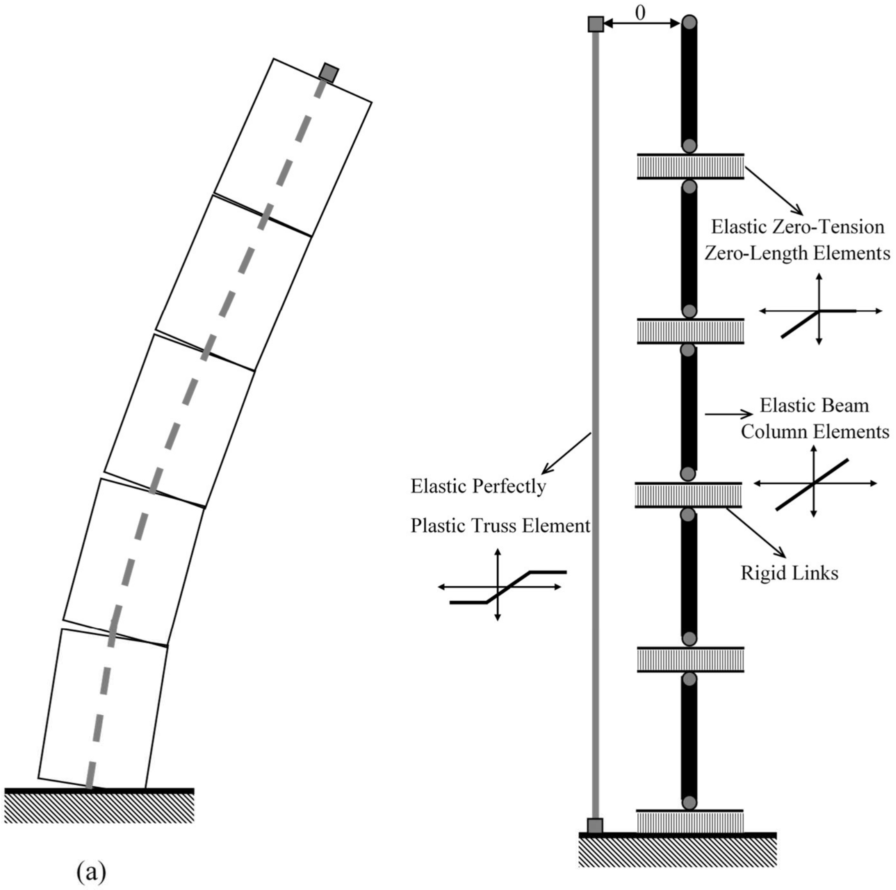

(a)

(b)

Figure 2. 2D FE modelling of the PPS piers in OpenSees programme.

The axial force of the top deck was exerted to the highest node of the piers. Moreover, lump horizontal and vertical masses at the highest node of the piers were used to account for inertial effects of the deck. The Lobatto Quadrature method was adopted to spread the vertical stiffness of the segments over the compression zones at the contact surfaces between the segments. Each compression zone (see Figure 2a) is modelled as a set of axial zero-length spring elements. An elastic zero-tension uniaxial material model is assigned to the joints, which can simulate the joint openings and compression forces at the contact surfaces. Further details on the FE model used and its experimental validation can be found in [47].

2.2 The equivalent RC pier

Figure 3 illustrates the equivalent RC pier to the PPS pier, C4, in this work. The equivalent RC and the PPS pier, C4, have similar initial elastic stiffness and ultimate strength. The RC pier is modelled using a five-node Nonlinear Fibre Beam-Column element.

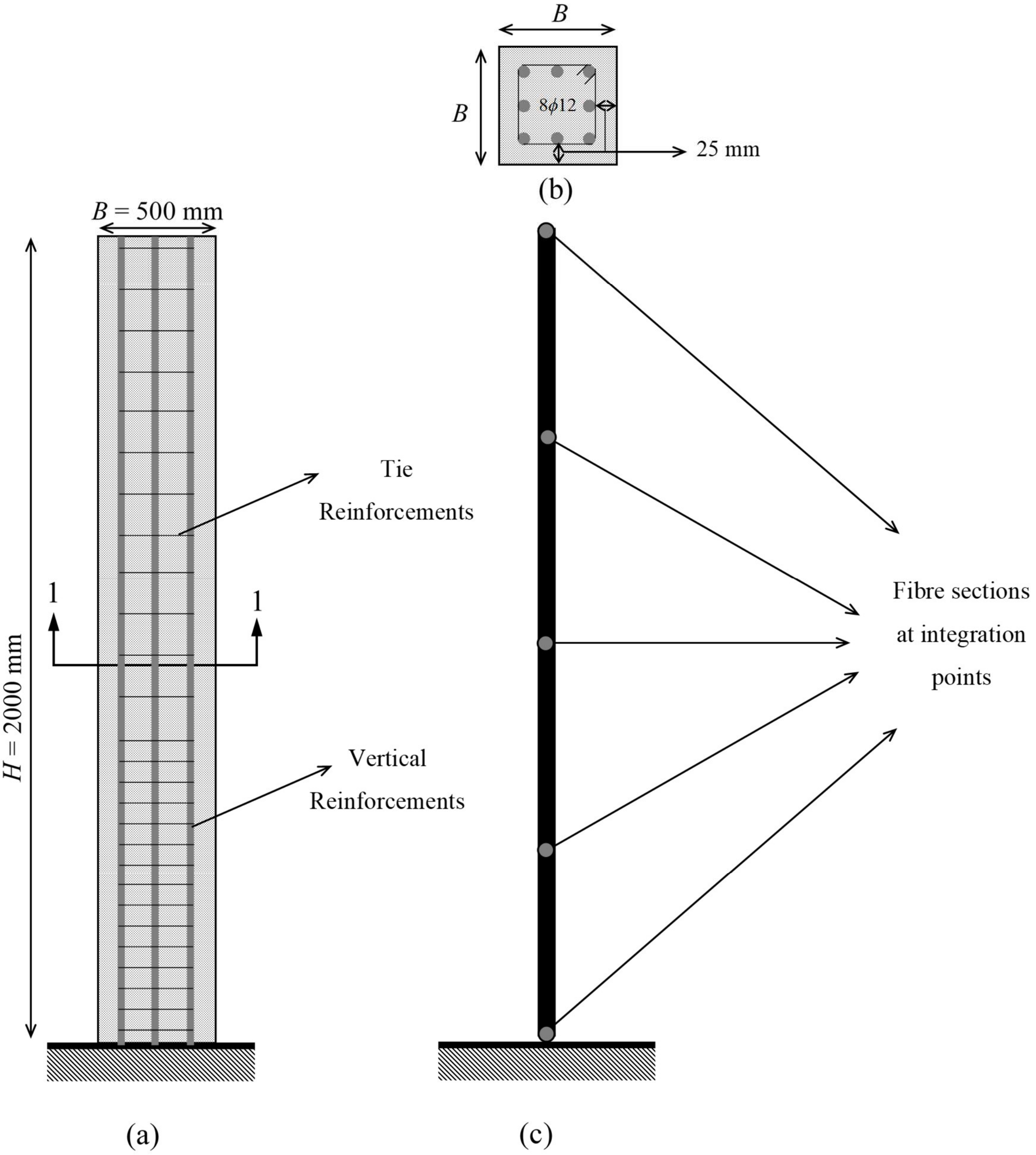

Figure 3. 2D FE modelling of the RC pier in OpenSees programme: (a) RC pier, (b) cross section of the pier, and (c) fibre-based FE model of the pier.

The reinforcing steel bars and concrete of the RC piers are simulated using Uniaxial Steel02 and Concrete02 in OpenSees programme, respectively. The ratio of strength of the confined core concrete to the unconfined cover concrete is taken 1.3. The cross section of the pier is divided into a number of fibres, and the specified uniaxial materials are separately assigned to each fibre. Uniaxial steel material of yield stress and elastic modulus of 420 MPa and 200 GPa are assigned to the reinforcing bars. Three reinforcement layers are used for the cross section of the pier (Figure 3b). The second order effects are incorporated into the model using P-Delta geometric transformation. To impose fixed condition at the base of the pier, all degrees of freedom of the bottom node are prevented. The same lumped masses as the PPS pier are assigned to the top node to account for inertial effects of the top deck.

3. The Ground Motion Database

A set of 44 far-fault ground motion records are used for the seismic assessment of the piers. Table 2 summarises specific properties of each ground motion. The ground motions are those recommended in FEMA P659 [50], and are composed of 22 component pairs of horizontal ground motions from sites located within a distance greater than 10 km from fault rupture. The set includes strong-motion records with peak ground acceleration (PGA) larger than 0.2g and peak ground velocity (PGV) larger than 15 cm/s from all large-magnitude (M>6.5) earthquakes available in the Pacific Earthquake Engineering Research Center (PEER) Next-Generation Attenuation (NGA) database [51]. The ground motions were recorded on soft rock and stiff soil sites (site class C and D conditions), and shallow crustal sources (mostly strike-slip and thrust mechanisms).

Table 2. Summary of PEER NGA database information and parameters of recorded far-field ground motions [50].

Ground Motion ID	PEER-NGA Record Information					
	Record Sequence No.	Lowest Frequency (Hz)	Component 1	Component 2	PGA_{max} (g)	PGV_{max} (cm/s)
1	953	0.25	NORTHR/MUL009	NORTHR/MUL279	0.52	63
2	960	0.13	NORTHR/LOS00	NORTHR/LOS270	0.48	45
3	1602	0.06	DUZCE/BOL000	DUZCE/BOL090	0.82	62
4	1787	0.04	HECTOR/HEC000	HECTOR/HEC090	0.34	42
5	169	0.06	IMPVALL/H-DLT262	IMPVALL/H-DLT352	0.35	33
6	174	0.25	IMPVALL/H-E11140	IMPVALL/H-E11230	0.38	42
7	1111	0.13	KOBE/NIS000	KOBE/NIS090	0.51	37
8	1116	0.13	KOBE/SHI000	KOBE/SHI090	0.24	38
9	1158	0.24	KOCAELI/DZC180	KOCAELI/DZC270	0.36	59
10	1148	0.09	KOCAELI/ARC000	KOCAELI/ARC090	0.22	40
11	900	0.07	LANDERS/YER270	LANDERS/YER360	0.24	52

12	848	0.13	LANDERS/CLW-LN	LANDERS/CLW-TR	0.42	42
13	752	0.13	LOMAP/CAP000	LOMAP/CAP090	0.53	35
14	767	0.13	LOMAP/G03000	LOMAP/G03090	0.56	45
15	1633	0.13	MANJIL/ABBAR--L	MANJIL/ABBAR--T	0.51	54
16	721	0.13	SUPERST/B-ICC00	SUPERST/B-ICC090	0.36	46
17	725	0.25	SUPERST/B-POE270	SUPERST/B-POE360	0.45	36
18	829	0.07	CAPEMEND/RIO270	CAPEMEND/RIO360	0.55	44
19	1244	0.05	CHICHI/CHY101-E	CHICHI/CHY101-N	0.44	115
20	1485	0.05	HICHI/TCU045-E	CHICHI/TCU045-N	0.51	39
21	68	0.25	SFERN/PEL090	SFERN/PEL180	0.21	19
22	125	0.13	FRIULI/A-TMZ000	FRIULI/A-TMZ270	0.35	31

4. Analysis and Results

4.1 IDA Analysis

The intensity measure (IM) selected for the IDA analysis in this study is the 5% damped spectral acceleration response at the pier's first mode period, S_a (T_1, 5%). T_1 is the first natural vibration period of the pier at very low-amplitude dynamic excitations where the joints are still close, no rocking motion has initiated. This period is determined using eigenvalue analysis of the piers. The first natural periods of the C2, C4, and C8 piers are 0.09s, 0.26s, and 0.75s respectively. Prior to the IDA analysis of each pier, the ground motions are first scaled to 1 at the natural period of each pier using their 5% damped spectra as shown in Figure 4. The ranges of the scale factor for C2, C4, and C8 are 0.76-4.52, 0.48-3.47, and 0.76-6.42 respectively. The IM is then changed from 0.05g to 1g with the increment of 0.05g. Small IM value of 0.005g very close to 0 is also considered to ensure elastic behaviour of the piers before their rocking initiation.

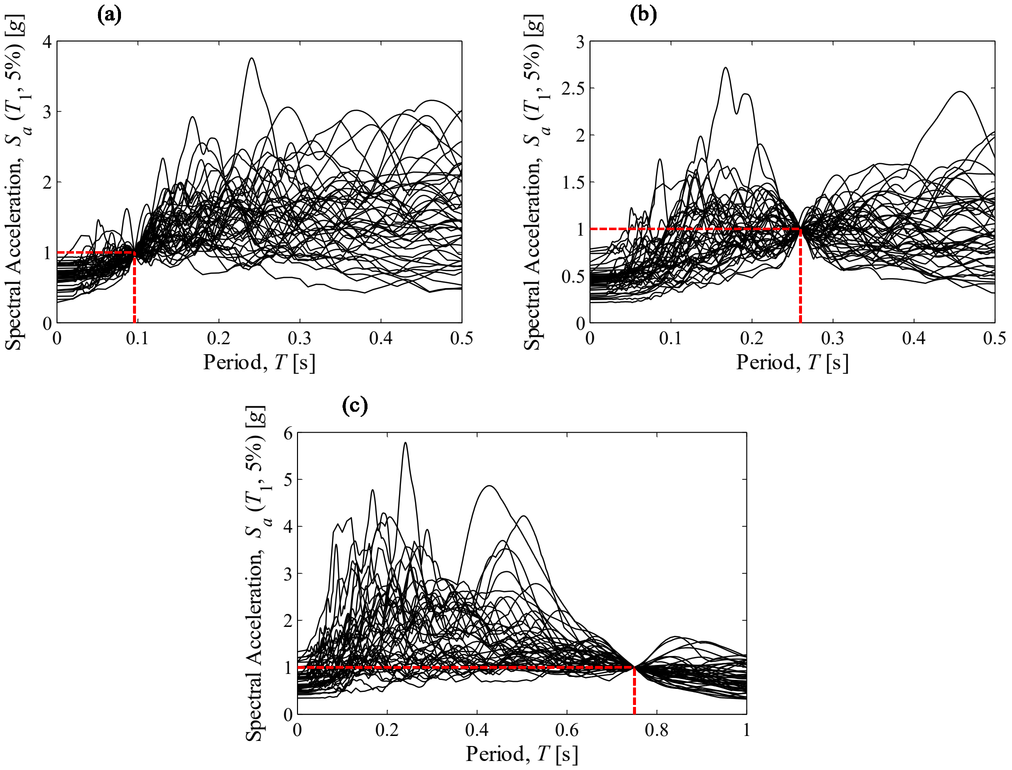

Figure 4. Scaling the ground motions to 1g at the period of the pier prior to the IDA analysis: (a) C2, (b) C4, and (c) C8.

Figure 5 illustrates auto spectral density (ASD) [52] of acceleration at the top of the piers normalised by their maximum values for IM values of 0.005g, 0.25g, and 0.5g subject to ground motion no. 10. The horizontal axes are frequency values normalised by the first natural frequency of each pier, f_1, at very low-amplitude excitations. The ASDs of the piers for IM = 0.005g exhibit very clear single peaks at roughly normalised frequency of 1 (see Figure 5a). This means that the piers have not started their rocking motion yet, and the joints are still close. For IM = 0.25g (Figure 5b), the C2 pier still vibrates around its natural frequency at very low-amplitude vibration given the maximum value of ASD around normalised frequency of 1. However, smaller ordinates of ASD at other frequencies show less contribution of subharmonics of the pier C2 [48]. For the slender and very slender piers, C4 and C8, the frequency of the fundamental mode drops which shows the joint opening and consequently the strength drop. Further, the slender and very slender piers have more clear subharmonics as expected [48]. For IM = 0.5g (Figure 5c), the base joint of the pier C2 opens, and a higher drop is seen in its strength compared to the other piers. Another interesting point is the higher frequency content of the pier C8 compared to the piers C2 and C4 at high IM values. The reason lies in the yielding of the post-tensioning tendon in the piers C2 and C4 which will be discussed later in following sections.

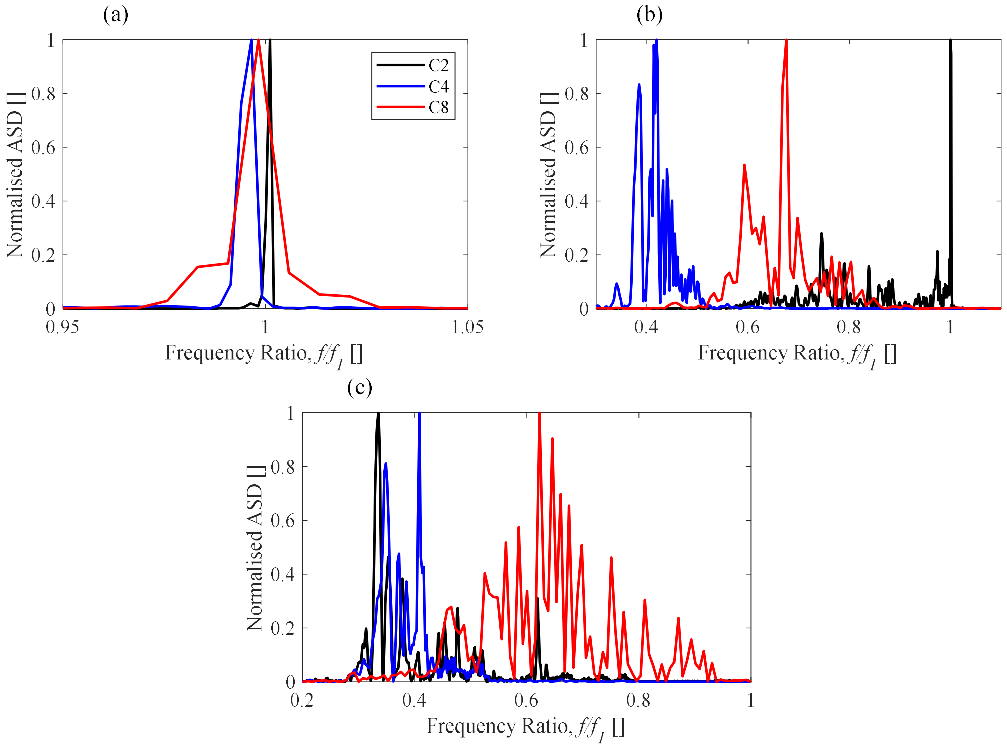

Figure 5. Normalised auto spectral density (ASD) of the top acceleration for the piers and different intensity measures subject to ground motion no 10: (a) 0.005g, (b) 0.25g, and (c) 0.5g.

Figure 6 shows hysteretic base shear versus displacement of the top of the piers for different values of intensity measures. The base shear is normalised by the total weight of the pier, *W*, (i.e. weight of the segments and the deck), and the top displacement is normalised by the height of the pier, i.e. top drift. At IM = 0.005g (Figure 6a), the piers remain elastic. The pier C2 is more stable, and requires higher minimum base excitation to start its rocking motion. Hence, its rocking starts at higher IM values compared to the other piers. The P-delta effects or second-order effects become very significant for the pier C8. As seen in Figures 6b and 6c, the strength of the pier C8 drop after drift ratio of around 0.01.

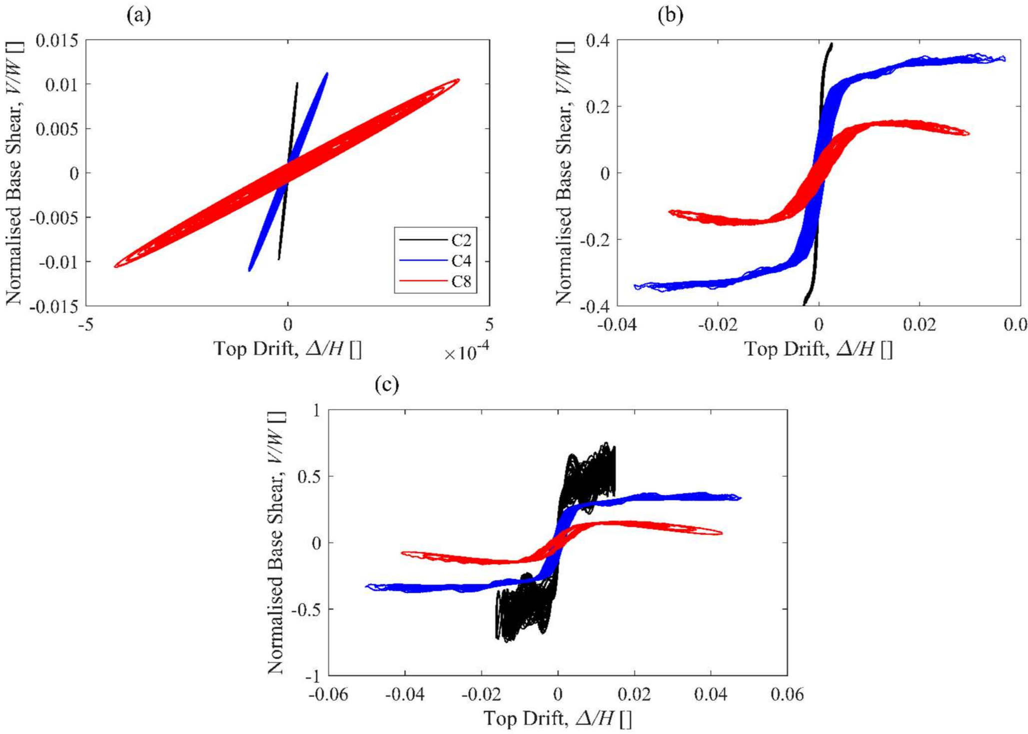

Figure 6. Normalised base shear versus top drift of the piers subject to ground motion 10: (a) 0.005g, (b) 0.25g, and (c) 0.5g.

4.2 IDA Curves

Maximum values of time history responses of the piers for each record and IM value are first determined. Then, the IM values are plotted versus maximum responses to produce IDA curves. The seismic responses considered in this study are drift, relative rotation, shear force, and moment at joint levels of the segments. Drift response at the joint level here is defined as the ratio of the lateral displacement at the joint level to the pier's height; relative rotation response is the absolute rotation of each segment subtracted by the rotation of the bottom segment; shear and moment responses are normalised by total weight (*W*) of the pier, and its gravitational moment (*BW*) respectively.

Figures 7-9 show exemplary IDA curves from ground motion 10 for drift, relative rotation, normalised shear, and moment at different joints across the piers. As expected, more slender pier gives higher drift ratio. For the squat pier, C2, the pier does not have rocking motion at very small IM values, and hence, the drift is very close to zero. For the piers C4 and C8, the rocking motion is started at very small IM values. The drift values increase with the increase of joint numbers which demonstrates the dominancy of the first mode as identical to a cantilever pier. The value of relative rotation reduces over the height of the pier.

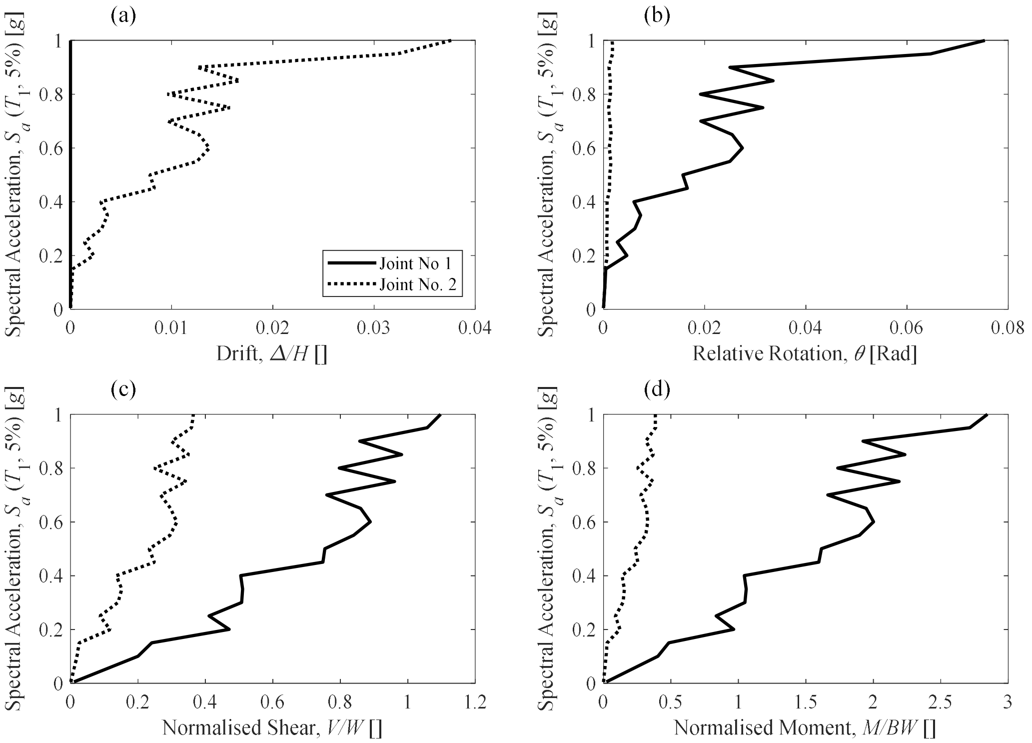

Figure 7. IDA curves of the pier C2 subject to ground motion 10 for the responses at the joints: (a) drift, (b) relative rotation, (c) normalised shear, and (d) normalised moment.

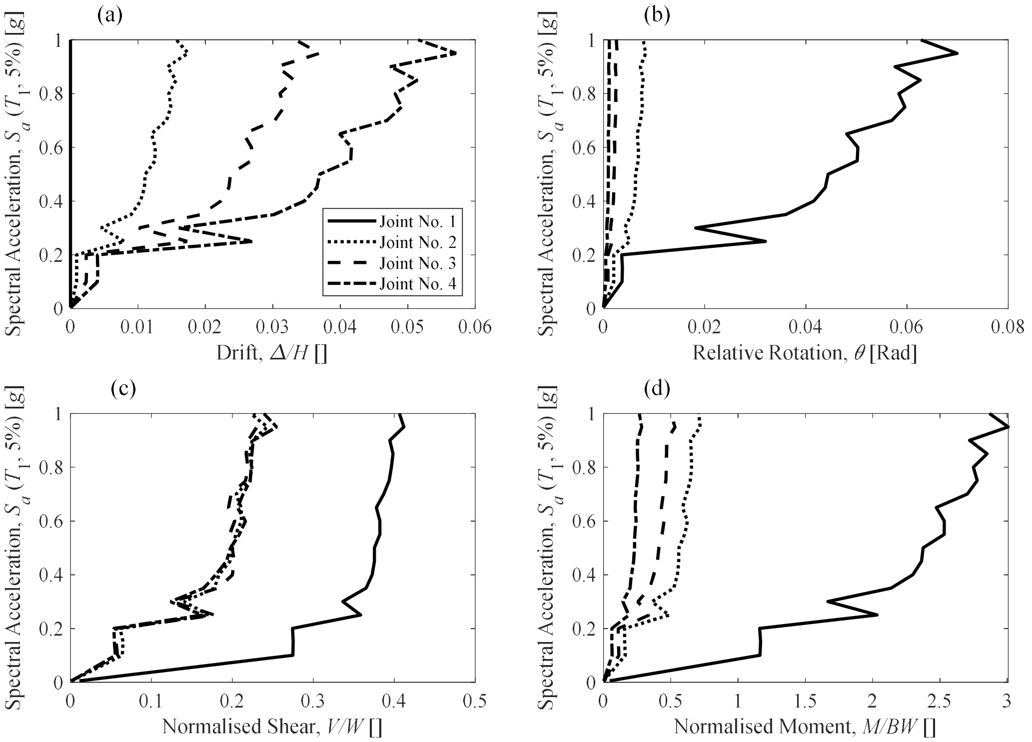

Figure 8. IDA curves of the pier C4 subject to ground motion 10 for the responses at the joints: (a) drift, (b) relative rotation, (c) normalised shear, and (d) normalised moment.

The base rotation is far larger than the rotation of the top joints for the piers C2 and C4. However, for the pier C8, the base joint and its adjacent joint have higher relative rotations. Like drift response, higher IM values will give higher relative rotation response. The value of the shear force is the largest by far at the base of the piers like a cantilever pier. Slenderising the pier also reduces the value of the shear force. The moment response follows the same trend as the shear force, and have its largest value at the base. The more slender the pier, the higher its moment value.

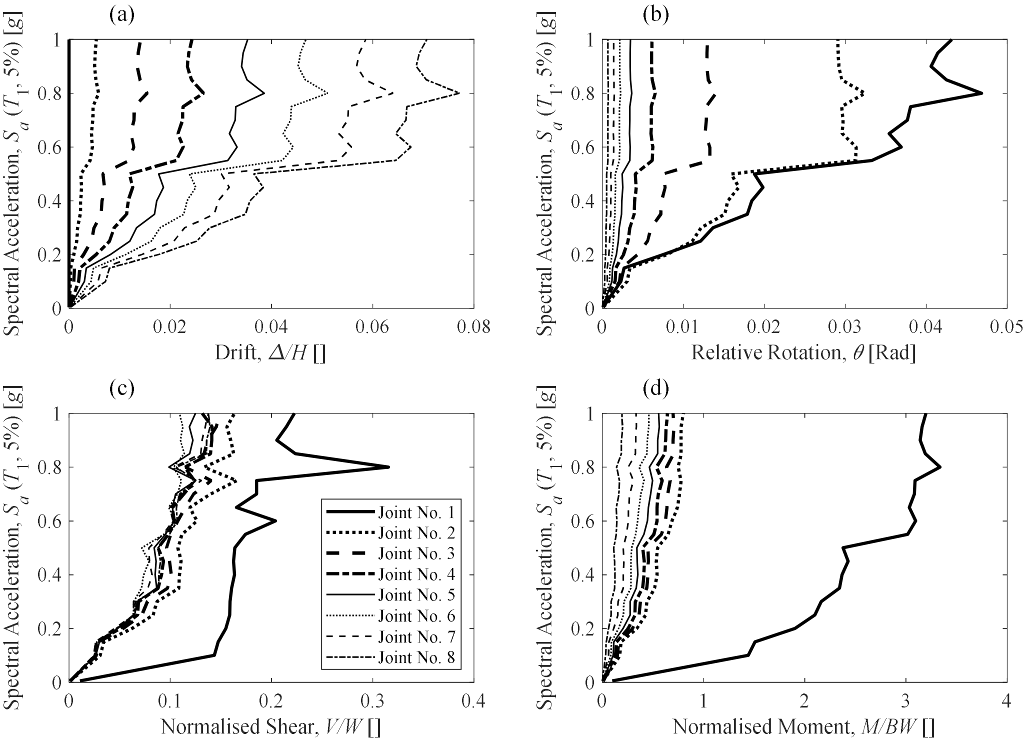

Figure 9. IDA curves of the pier C8 subject to ground motion 10 for the responses at the joints: (a) drift, (b) relative rotation, (c) normalised shear, and (d) normalised moment.

Figure 10 shows the IDA curves for all of the ground motions as well as their median IDA curve for top drift, base rotation, base shear, and base moment response of the pier C4. The median of all responses increase with the increase of IM values. The variation of median top drift and median base rotation is very slight at small IM values as the joints have not been opened yet. At higher IM values, the change in the median top drift and base rotation becomes larger for post-opening phase of the joints. Conversely, the variation of median base shear and median base moment is large at small IM values (pre-opening phase of the joints), and it becomes smaller for higher IM values (post-opening phase of the joints) as the contact surfaces are smaller.

Figure 11 compares median IDA curves of all three piers for various responses. For small IM values, as the pier becomes more slender, the top drift becomes larger (see Figure 11a). The reason lies in the fact that slender piers require smaller minimum ground excitation to start their rocking motion. However, at higher IM values, the squat pier gives higher top drift as all the piers have initiated their rocking motion. The median IDA curves of the base rotation exhibit the same trend as the top drift (Figure 11b). The only difference is the IM value at which the effect of the aspect ratio becomes reversed. This IM value is larger for the top drift.

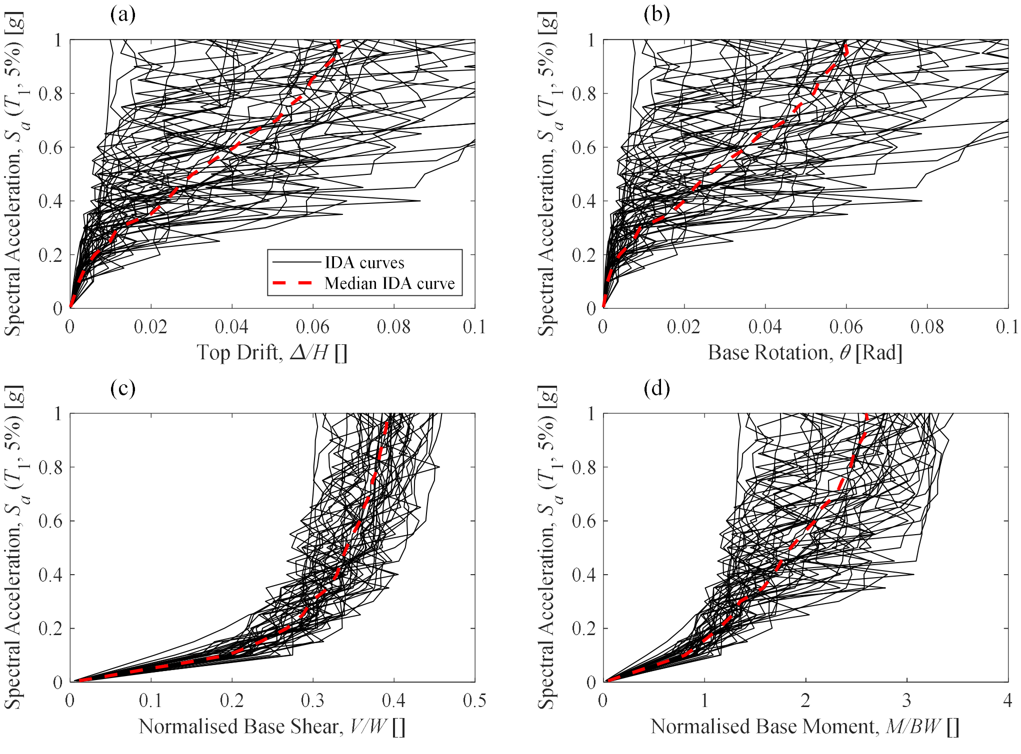

Figure 10. IDA curves and median IDA curve of the pier C4 subject to all ground motions for: (a) top drift, (b) base rotation, (c) normalised base shear, and (d) normalised base moment.

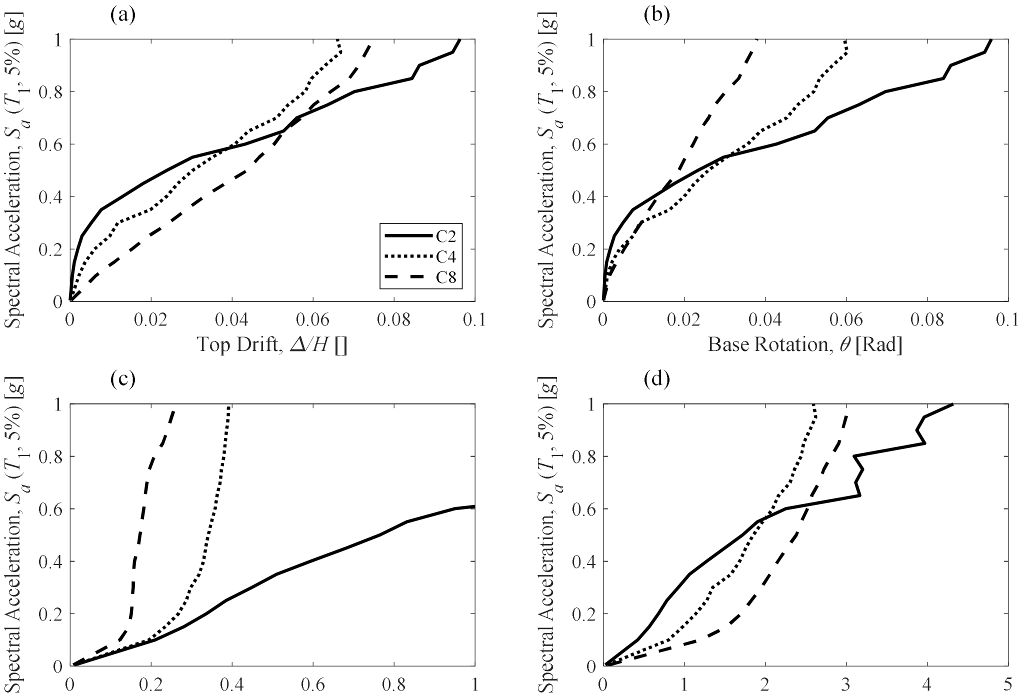

Figure 11. Median IDA curves of all ground motions for the piers: (a) top drift, (b) base rotation, (c) normalised base shear, and (d) normalised base moment.

At small IM values, the slope of the median IDA curves for the base shear are very similar as they have similar area of contact at the joints (Figure 11c). However, the squat pier possesses the largest amount of base shear at all IM values. Particularly for the piers C4 and C8, the base shear becomes approximately constant for large IM values as their median IDA curves approach vertical lines. The median IDA curves of the base moment follow a similar trend to the top drift and base rotation. Again, there is an IM value at which the effect of the pier's aspect ratio becomes reversed. Below this IM, the more slender pier gives higher base moment. However, above this IM value, the squat pier gives larger base moment. Figure 12a illustrates IDA curves of the pier C4 and its median IDA curve for the post-tensioning stress of the tendon normalised by its yielding stress. Figure 12b compares median IDA curves of the piers for the normalised post-tensioning force of the tendon. The drop in the initial tendon force ratio is because of the tension loss due to elastic shortening of the segments as well as the flexibility of rocking surfaces under gravity loads. This tension loss is higher for the more slender piers as they have more number of segments and joints. The post-tensioning force of the tendon is approximately constant for very small IM values (pre-opening phase of the joints), and it increases as the rotation of the joints increases (post-opening phase). Further, the squat pier results in a far larger post-tensioning force in the tendon compared to other piers, and the tendon of the squat pier, C2, yields at very high IM levels while the other two piers remain elastic.

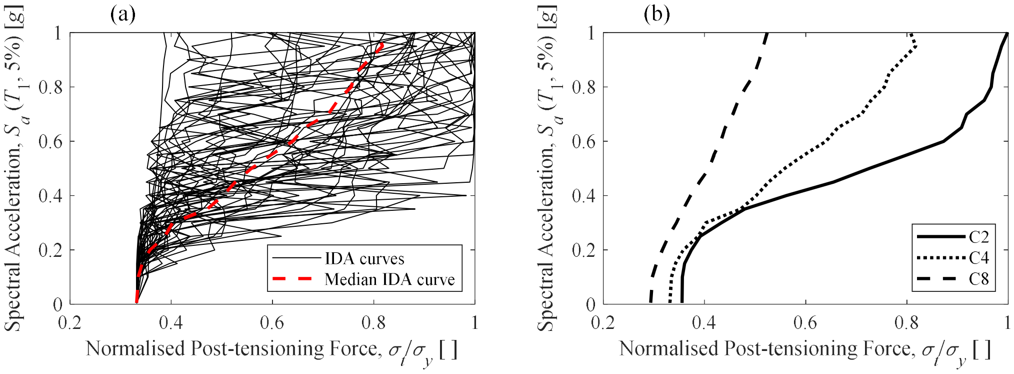

Figure 12. Normalised post-tensioning force of the tendon: (a) IDA curves and median IDA curve of the pier C4, and (b) median IDA curves for the piers.

Figure 13 shows the IDA curves of the RC pier for the top drift and normalised base shear. The less dispersion of the IDA curves for the base shear (see Figure 13b) shows the fact that the pier becomes very soft, i.e. very large strength drop after the yielding of the reinforcing bars (this will be discussed more in section 4.3 and Figure 17a). This leads to a very flexible pier (long-period pier), and consequently an almost constant base shear. Figure 14 compares the median curves of the RC pier and the PPS pier, C4. For the same IM level, the RC pier exhibits less top drift and base shear compared to the PPS pier. The PPS pier loses strength after rocking of the segments subject to a base excitation, and this leads to a higher drift compared to the RC pier where the column is still very stiff before the yielding of the steel bars.

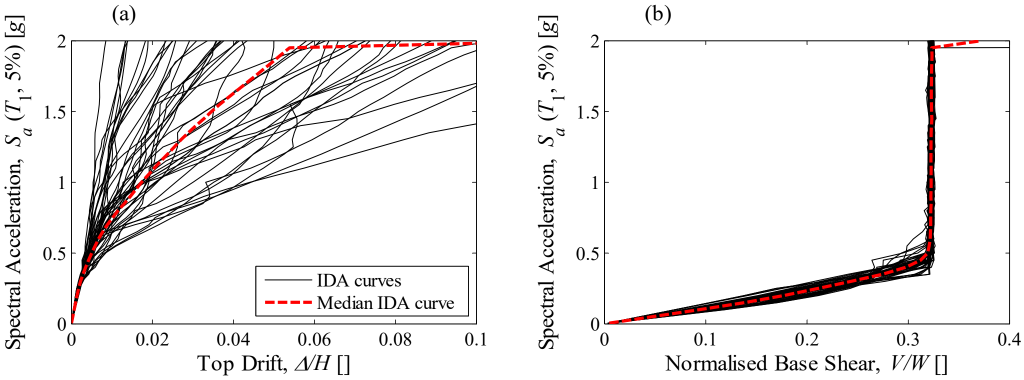

Figure 13. IDA curves and median IDA curve of the RC pier: (a) top drift, and (b) normalised base shear.

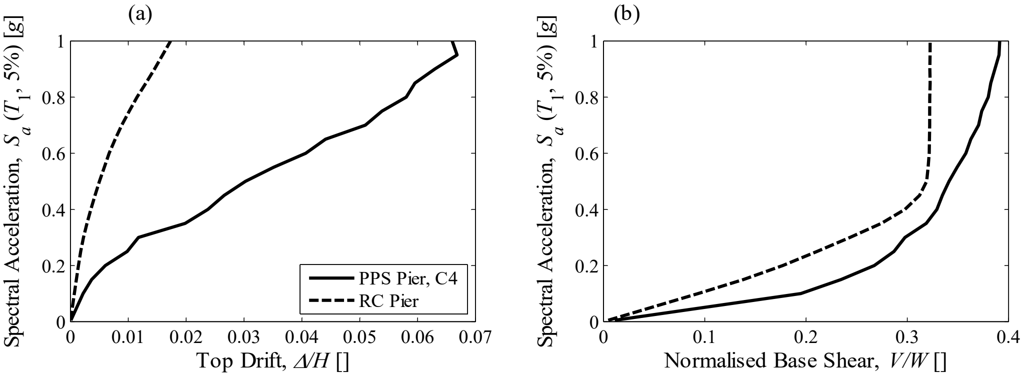

Figure 14. Median IDA curves of the PPS pier, C4 and RC pier: (a) drift, and (b) normalised base shear.

4.3 Fragility Curves

As seen in the previous section, the IDA analyses cover a wide range of IM levels allowing simulation of the pier's seismic behaviour from the initial healthy state to the collapse state. The results of the IDA analyses, presented in section 4.2, are used herein to develop fragility curves for the piers C2, C4, and C8. The fragility curves quantify the probability of exceeding a given damage/performance state. The fragility function is often expressed as a standard lognormal cumulative distribution function:

$$P\left(DS \geq ds \mid IM = x\right) = \phi\left(\frac{\ln(x) - \ln(\theta)}{\beta}\right) \tag{1}$$

where $P\left(DS \geq ds \mid IM = x\right)$ is the probabiity which a ground motion of $IM = x$ results in a particular damage state equal or larger than ds; ϕ is the standard lognoraml distrbution function; θ and β are the median and logarithmic standard deviation of the fragility function, respectively. The moment estimator method is used to determine θ and β:

$$\ln(\theta) = \frac{1}{N}\sum_{i=1}^{N}\ln(IM_i) \tag{2}$$

$$\beta = \sqrt{\frac{1}{N-1}\sum_{i=1}^{N}\left(\ln(IM_i) - \ln(\theta)\right)^2} \tag{3}$$

in which, N is the number of ground motions used for IDA analysis and IM_i is the IM level at which the damage state starts.

To determine fragility curves, damage limit states need be identified and defined for the PPS piers. Two potential failure can be considered for the PPS piers: (1) as the post-tensioning tendon provides global stability and self-centring capacity of the PPS piers, yielding of the tendon will lead to collapse of such piers, and (2) also, like the CIP piers, extensive strength drop of the PPS piers can happen due to the second order or P-delta effects. Hence, Slight, Moderate, and Extensive Damage states are defined where the tendon stress reaches $0.5\sigma_y$, $0.7\sigma_y$, and $0.9\sigma_y$, respectively. Furthermore, it is assumed that the Extensive Damage begins when the strength loss of the piers reaches 20%.

To investigate the above possible failure mechanisms, post-tensioning force of the tendon and base shear of the piers are determined using pushover analysis (see Figure 15). For the pier C2, the tendon stress reaches $0.5\sigma_y$, $0.7\sigma_y$, and $0.9\sigma_y$ at the top drift values of 0.01, 0.02, and 0.03 respectively for damage states of Slight, Moderate, and Extensive (Figure 15b). These values are far less than the top drift value of 0.09 where the 20% strength loss of the pier C2 occurs (Figure 15a). For the pier C4, the top drifts corresponding to the tendon stress limits are 0.025, 0.05, and 0.07 (Figure 15b) which are equal or less than 0.07 where the 20% strength loss occurs (Figure 15a). Thus, for the piers C2 and C4, yielding of the tendon is the dominant failure mode. For the pier C8, however, the top drifts from the tendon stress limits are 0.075, 0.14, and 0.21 (Figure 15b) which are far higher than 0.028 where the 20% strength loss happens (Figure 15a). Thus, for the pier C8, the 20% strength loss governs the damage state due to high amount of second order or P-delta effects. Hence, for the pier C8, only Extensive Damage state is defined at drift of 0.028 to be compared to the other two piers. Given strength drop of very slender PPS piers at small drift values, they are not recommended for medium to high seismic regions.

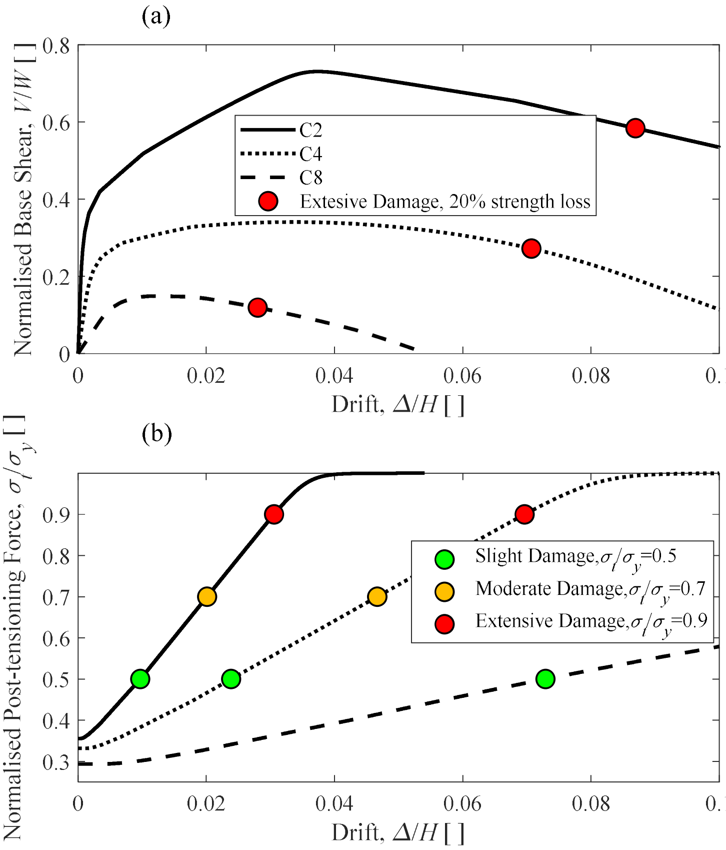

Figure 15. Pushover analysis of the piers: (a) normalised base shear versus drift curves, and (b) normalised post-tensioning force versus top drift curves.

Figure 16 illustrates the fragility curves for the piers at different damage states. For the Slight Damage state, the pier C2 reaches probability of exceedance 0.9 at IM values of 0.53g while it occurs at IM value of 0.75g for the pier C4. In case of Moderate Damage state, probability of exceedance of 0.9 is attained at IM value of 0.68g and 1.1g respectively for the piers C2 and C4. The IM values corresponding to probability of exceedance of 0.9 for the Extensive Damage state are 0.8g and 1.25g respectively for the piers C2 and C4. The slender pier, C4, exhibits a better seismic performance compared to the squat pier C2. However, the aspect ratio of the pier must be limited so that the yielding of the tendon occurs prior to the strength loss of the pier.

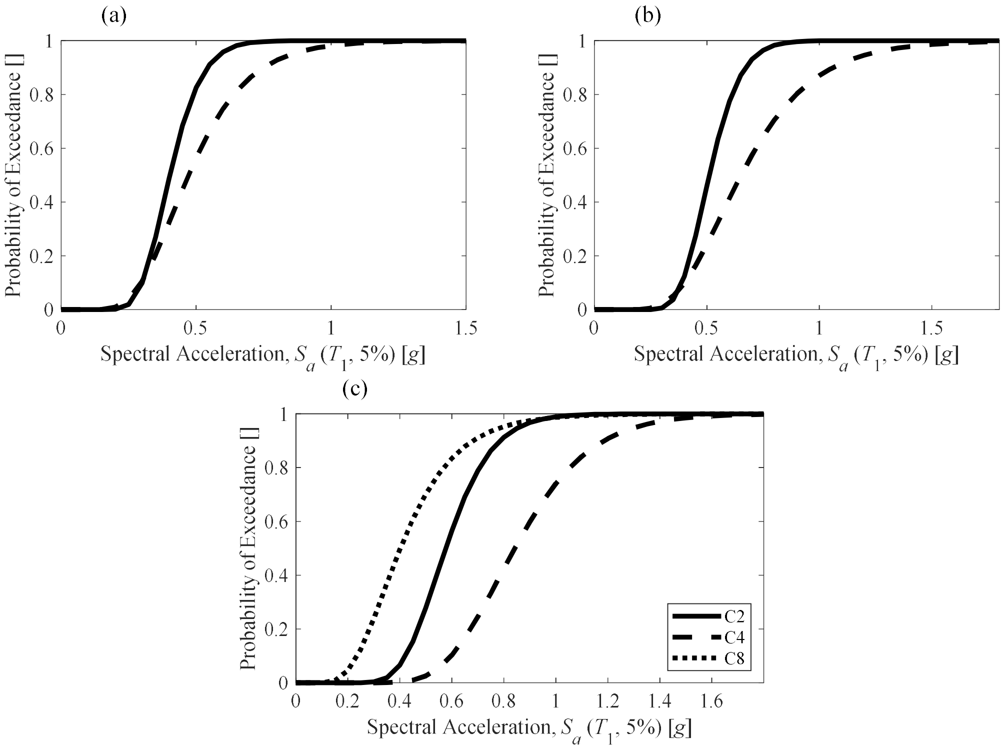

Figure 16. Fragility curves of the piers C2, C4, and C8: (a) Slight Damage, (b) Moderate Damage, and (c) Extensive Damage.

In contrast to a PPS pier, an RC pier has completely different failure modes: (1) spalling of cover concrete, (2) crushing of core concrete, (3) yielding of vertical reinforcing bars, and (4) fracture of vertical reinforcing bars ([53], (Dizaj et al. 2018)). Figure 17 shows the pushover analysis results of the RC pier in this work. The material strains corresponding to the spalling of cover concrete, crushing of core concrete, yielding and fracture of the reinforcing bars are 0.003, 0.087, 0.002, and 0.15 respectively (see Figure 17b). The top drifts, at which these material strains are reached, are 0.004, 0.07, 0.007, and 0.06 (see Figure 17a). Thus, the reinforcing bars first yield, the cover concrete then spalls, and the core concrete crushes before the fracture of the reinforcing bars. Herein, to compare with the PPS piers, yielding of the reinforcing bar, spalling of cover concrete, and crushing of the core concrete are taken as Slight Damage, Medium Damage, and Extensive Damage states. Figure 18 compares the fragility curves of the RC pier and the PPS pier, C4. For the Slight Damage state (see Figure 18a), probability of exceedance of 0.9 is attained at a lower IM value for the RC pier compared to the PPS pier, C4, while for the Moderate Damage state, the IM value corresponding to the probability of exceedance of 0.9 is similar for both piers (see Figure 18b). However, for the Extensive Damage state, the IM value for a specific probability of exceedance occurs at IM values far higher for the RC pier (see Figure 18c). This means the collapse probability of an RC pier is lower than a PPS pier.

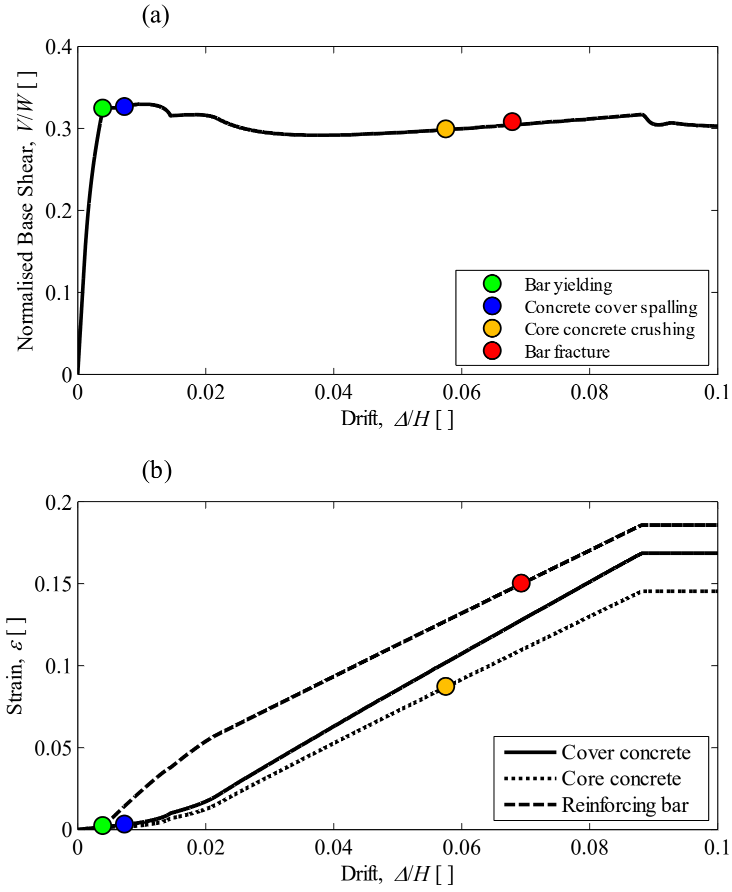

Figure 17. Pushover analysis of the RC pier: (a) normalised base shear versus drift curves, and (b) concrete and steel strain versus top drift curves.

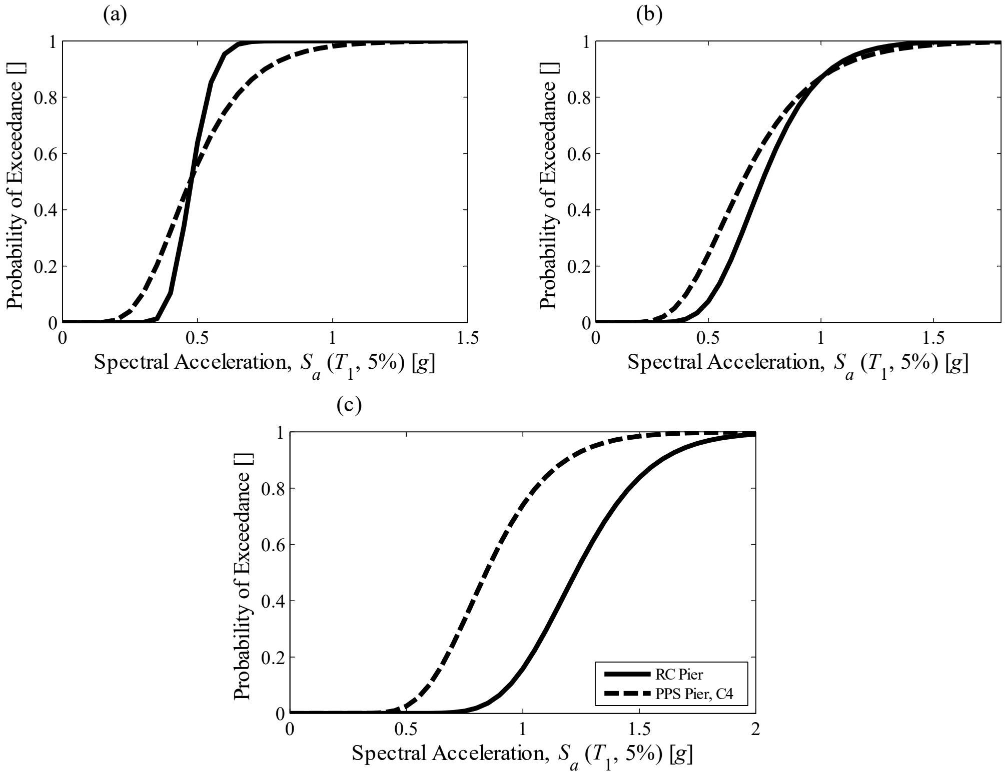

Figure 18. Fragility curves of the RC pier versus the PPS pier, C4: (a) Slight Damage, (b) Moderate Damage, and (c) Extensive Damage.

5. Conclusions

In this study, seismic performance of precast post-tensioned segmental piers are investigated using IDA analyses. An experimentally validated FE model is used to simulate dynamic behaviour of three piers with different aspect ratios subject to an extensive ensemble of 44 far-fault ground motions. IDA curves, median IDA curves, and fragility curves were then determined to perform seismic assessment of the piers.

The IDA curves demonstrated that the maximum relative rotation, shear force, and moment responses occur at the base of the piers, and also, the responses increases as the ground motion intensity increases. It was found from the median IDA curves of the piers that slenderising the pier increases the top drift, base rotation, and base moment. However, there is an intensity measure above which, the trend becomes reversed. Such intensity measure, however, was not seen for the base shear, and the base shear continuously reduced as the pier became more slender.

Two failure criteria of yielding of the tendon and global strength loss were identified for the piers. It was found that slender piers exhibit fragility curves stretched towards higher intensity measures which shows better seismic performance of slender piers. However, an upper limit must be placed on the slenderness of the piers as global strength loss might lead to their failure at very small drift values. Comparing the fragility curves of the PPS pier and its equivalent RC pier demonstrated that the collapse probability of the PPS piers are higher.

Acknowledgement

The authors acknowledge the support received by the UK Engineering and Physical Sciences Research Council (EPSRC) for a Prosperous Nation [grant number EP/R039178/1]**:** *SPINE: Resilience-Based Design of Biologically Inspired Columns for Next-Generation Accelerated Bridge Construction*].

References

[1] Kashani MM, Lowes LN, Crewe AJ, Alexander NA. Computational modelling strategies for nonlinear response prediction of corroded circular RC bridge piers. Adv Mater Sci Eng 2016;2016. https://doi.org/10.1155/2016/2738265.

[2] Ni Choine M, Kashani MM, Lowes LN, O'Connor A, Crewe AJ, Alexander NA, et al. Nonlinear dynamic analysis and seismic fragility assessment of a corrosion damaged integral bridge. Int J Struct Integr 2016;7:227–39. https://doi.org/10.1108/IJSI-09-2014-0045.

[3] Kashani MM, Alagheband P, Khan R, Davis S. Impact of corrosion on low-cycle fatigue degradation of reinforcing bars with the effect of inelastic buckling. Int J Fatigue 2015;77:174–85. https://doi.org/10.1016/j.ijfatigue.2015.03.013.

[4] Rahgozar N, Moghadam AS, Aziminejad A. Quantification of seismic performance factors for self-centering controlled rocking special concentrically braced frame. Struct Des Tall Spec Build 2016. https://doi.org/10.1002/tal.1279.

[5] Steele TC, Wiebe LDA. Collapse risk of controlled rocking steel braced frames with different post-tensioning and energy dissipation designs. Earthq Eng Struct Dyn 2017. https://doi.org/10.1002/eqe.2892.

[6] Spanos BPD, Koh A. Rocking of rigid blocks due to harmonic shaking. ASCE, J Eng Mech 1985;110:1627–42.

[7] Spanos PD, Koh AS. Analysis of block random rocking. Soil Dyn Earthq Eng 1986;5:178–83. https://doi.org/10.1016/0267-7261(86)90021-7.

[8] Shenton HW, Jones NP. Base Excitation of Rigid Bodies. I: Formulation. J Eng Mech 1991;117:2286–306. https://doi.org/10.1061/(ASCE)0733-9399(1991)117:10(2286).

[9] Shenton HW, Jones NP. Base excitation of rigid bodies. II: Periodic slide-rock response. J Eng Mech 1991;117:2307–28. https://doi.org/10.1061/(ASCE)0733-9399(1991)117:10(2307).

[10] Kounadis AN. Parametric study in rocking instability of a rigid block under harmonic ground pulse: A unified approach. Soil Dyn Earthq Eng 2013;45:125–43. https://doi.org/10.1016/j.soildyn.2012.10.002.

[11] Dimitrakopoulos EG, DeJong MJ. Revisiting the rocking block: Closed-form solutions and similarity laws. Proc. R. Soc. A Math. Phys. Eng. Sci., vol. 468, 2012, p. 2294–318. https://doi.org/10.1098/rspa.2012.0026.

[12] Yim C -S, Chopra AK, Penzien J. Rocking response of rigid blocks to earthquakes. Earthq Eng Struct Dyn 1980;8:565–87. https://doi.org/10.1002/eqe.4290080606.

[13] Aslam M, Godden WG, Scalise DT. Earthquake Rocking Response of Rigid Bodies. J Struct Div 1980;106:377–92.

[14] Pompei A, Scalia A, Sumbatyan MA. Dynamics of Rigid Block due to Horizontal Ground Motion. J Eng Mech 1998;124:713–7. https://doi.org/10.1061/(asce)0733-9399(1998)124:7(713).

[15] DeJong MJ, Dimitrakopoulos EG. Dynamically equivalent rocking structures. Earthq Eng Struct Dyn 2014;43:1543–63. https://doi.org/10.1002/eqe.2410.

[16] Kounadis AN. On the rocking-sliding instability of rigid blocks under ground excitation: some new findings. Soil Dyn Earthq Eng 2015;75:246–58. https://doi.org/10.1016/j.soildyn.2015.03.026.

[17] Kounadis AN, Papadopoulos GJ. On the rocking instability of a three-rigid block system under ground excitation. Arch Appl Mech 2016;86:957–77. https://doi.org/10.1007/s00419-015-1073-9.

[18] Kounadis AN. The effect of sliding on the rocking instability of multi- rigid block assemblies under ground motion. Soil Dyn Earthq Eng 2018;104:1–14. https://doi.org/10.1016/j.soildyn.2017.03.035.

[19] Makris N, Vassiliou MF. The dynamics of the rocking frame. Comput. Methods Appl. Sci., vol. 37, 2015, p. 37–59. https://doi.org/10.1007/978-3-319-16130-3-2.

[20] Billington SL, Yoon JK. Cyclic response of unbonded posttensioned precast columns with ductile fiber-reinforced concrete. J Bridg Eng 2004. https://doi.org/10.1061/(ASCE)1084-0702(2004)9:4(353).

[21] Hassanli R, Youssf O, Mills JE. Seismic performance of precast posttensioned segmental FRP-Confined and unconfined crumb rubber concrete columns. J Compos Constr 2017. https://doi.org/10.1061/(ASCE)CC.1943-5614.0000789.

[22] Wang J, Wang Z, Tang Y, Liu T, Zhang J. Cyclic loading test of self-centering precast segmental unbonded posttensioned UHPFRC bridge columns. Bull Earthq Eng 2018. https://doi.org/10.1007/s10518-018-0331-y.

[23] Wang Z, Wang J, Zhu J. Pushover analysis of precast segmental UHPFRC bridge columns with unbonded posttensioned tendons. Key Eng. Mater., 2018. https://doi.org/10.4028/www.scientific.net/KEM.765.391.

[24] Hewes JT. Seismic design and performance of precast concrete segmental bridge columns. 2002. https://doi.org/10.1016/S0165-0327(00)00241-X.

[25] Ou YC, Chiewanichakorn M, Aref AJ, Lee GC. Seismic performance of segmental precast unbonded posttensioned concrete bridge columns. J Struct Eng 2007. https://doi.org/10.1061/(ASCE)0733-9445(2007)133:11(1636).

[26] Chou CC, Chen YC. Cyclic tests of post-tensioned precast CFT segmental bridge columns with unbonded strands. Earthq Eng Struct Dyn 2006. https://doi.org/10.1002/eqe.512.

[27] Marriott D, Pampanin S, Palermo A. Quasi-static and pseudo-dynamic testing of unbonded post-tensioned rocking bridge piers with external replaceable dissipaters. Earthq Eng Struct Dyn 2009;38:331–54. https://doi.org/10.1002/eqe.857.

[28] Elgawady MA, Sha'Lan A. Seismic behavior of self-centering precast segmental bridge bents. J Bridg Eng 2011. https://doi.org/10.1061/(ASCE)BE.1943-5592.0000174.

[29] Ou YC, Tsai M Sen, Chang KC, Lee GC. Cyclic behavior of precast segmental concrete bridge columns with high performance or conventional steel reinforcing bars as energy dissipation bars. Earthq Eng Struct Dyn 2010;39:1181–98. https://doi.org/10.1002/eqe.986.

[30] Motaref S, Saiidi MS, Sanders DH. Experimental study of precast bridge columns with built-in elastomer. Transp Res Rec 2010. https://doi.org/10.3141/2202-14.

[31] Sideris P, Aref AJ, Filiatrault A. Large-scale seismic testing of a hybrid sliding-rocking posttensioned segmental bridge system. J Struct Eng (United States) 2014. https://doi.org/10.1061/(ASCE)ST.1943-541X.0000961.

[32] Sideris P, Aref AJ, Filiatrault A. Experimental seismic performance of a hybrid sliding-rocking bridge for various specimen configurations and seismic loading conditions. J Bridg Eng 2015. https://doi.org/10.1061/(ASCE)BE.1943-5592.0000742.

[33] Kashani MM, Gonzalez-Buelga A. Nonlinear dynamics of self-centring segmental composite rocking column. Procedia Eng., 2017. https://doi.org/10.1016/j.proeng.2017.09.176.

[34] Kashani MM, Gonzalez-Buelga A, Thayalan RP, Thomas AR, Alexander NA. Experimental investigation of a novel class of self-centring spinal rocking column. J Sound Vib 2018. https://doi.org/10.1016/j.jsv.2018.08.034.

[35] Kashani MM, Ahmadi E, Gonzalez-Buelga A, Zhang D, Scarpa F. Layered composite entangled wire materials blocks as pre-tensioned vertebral rocking columns. Compos Struct 2019. https://doi.org/10.1016/j.compstruct.2019.02.021.

[36] Ahmadi E, Kahshani MM. On the use of entangled wire materials in pre-tensioned rocking columns. XIIIth Int. Conf. Recent Adv. Struct. Dyn. Inst. Sound Vib. Res. (ISVR), Lyon, Fr., 2019.

[37] Zhang X, Hao H. The response of precast concrete segmental columns subjected to near base impact. Int J Prot Struct 2019. https://doi.org/10.1177/2041419618808534.

[38] Dawood H, Elgawady M, Hewes J. Behavior of segmental precast posttensioned bridge piers under lateral loads. J Bridg Eng 2012. https://doi.org/10.1061/(ASCE)BE.1943-5592.0000252.

[39] Do T V., Pham TM, Hao H. Numerical investigation of the behavior of precast concrete segmental columns subjected to vehicle collision. Eng Struct 2018. https://doi.org/10.1016/j.engstruct.2017.11.033.

[40] ElGawady MA, Dawood HM. Analysis of segmental piers consisted of concrete filled FRP tubes. Eng Struct 2012. https://doi.org/10.1016/j.engstruct.2012.01.001.

[41] Motaref S. Seismic Response of Precast Bridge Columns with Energy Dissipating Joints. 2011.

[42] Zhang N. Dynamic properties and application of steel fiber reinforced self-consolidating concrete to segmental bridge columns in moderate-to-high seismic regions. 2014.

[43] Lee WK, Billington SL. Modeling Residual Displacements of Concrete Bridge Columns under Earthquake Loads Using Fiber Elements. J Bridg Eng 2010;15:240–9.

https://doi.org/10.1061/(ASCE)BE.1943-5592.0000059.

[44] Abdel Raheem SE. Pounding mitigation and unseating prevention at expansion joints of isolated multi-span bridges. Eng Struct 2009;31:2345–56. https://doi.org/10.1016/j.engstruct.2009.05.010.

[45] Shrestha B, Hao H, Bi K. Effectiveness of using rubber bumper and restrainer on mitigating pounding and unseating damage of bridge structures subjected to spatially varying ground motions. Eng Struct 2014;79:195–210. https://doi.org/10.1016/j.engstruct.2014.08.020.

[46] Cai ZK, Zhou Z, Wang Z. Influencing factors of residual drifts of precast segmental bridge columns with energy dissipation bars. Adv Struct Eng 2019. https://doi.org/10.1177/1369433218780545.

[47] Ahmadi E, Kashani MM. Numerical investigation of nonlinear static and dynamic behaviour of self-centring rocking segmental bridge piers. Soil Dyn Earthq Eng 2020;128:105876. https://doi.org/10.1016/j.soildyn.2019.105876.

[48] McKenna F. OpenSees: A framework for earthquake engineering simulation. Comput Sci Eng 2011. https://doi.org/10.1109/MCSE.2011.66.

[49] Vamvatsikos D, Allin Cornell C. Incremental dynamic analysis. Earthq Eng Struct Dyn 2002. https://doi.org/10.1002/eqe.141.

[50] FEMA P695. Quantification of Building Seismic Performance Factors. 2009.

[51] Pacific Earthquake Engineering Research Center. PEER Ground Motion Database. Shallow Crustal Earthquakes Act Tecton Regimes, NGA-West2 2017.

[52] Chatfield C, Bendat JS, Piersol AG. Random Data: Analysis and Measurement Procedures. J R Stat Soc Ser A 1987. https://doi.org/10.2307/2981634.

[53] Dizaj EA, Madandoust R, Kashani MM. Probabilistic seismic vulnerability analysis of corroded reinforced concrete frames including spatial variability of pitting corrosion. Soil Dyn Earthq Eng 2018;114:97–112. https://doi.org/10.1016/j.soildyn.2018.07.013.

[54] Afsar Dizaj E, Madandoust R, Kashani MM. Exploring the impact of chloride-induced corrosion on seismic damage limit states and residual capacity of reinforced concrete structures. Struct Infrastruct Eng 2018;14:714–29. https://doi.org/10.1080/15732479.2017.1359631.